

Novel structures and mechanical properties of Zr_2N: *Ab initio* description under high pressures

Minru Wen(文敏儒), Xing Xie(谢兴), Zhixun Xie(谢植勋), Huafeng Dong(董华锋), Xin Zhang(张欣), Fugen Wu(吴福根), and Chong-Yu Wang(王崇愚)

Citation: Chin. Phys. B, 2021, 30 (**1**): 016403. DOI: 10.1088/1674-1056/abb220
Journal homepage: http://cpb.iphy.ac.cn; http://iopscience.iop.org/cpb

What follows is a list of articles you may be interested in

Temperature-induced phase transition of two-dimensional semiconductor GaTe

Xiaoyu Wang(王啸宇), Xue Wang(王雪), Hongshuai Zou(邹洪帅), Yuhao Fu(付钰豪), Xin He(贺欣), and Lijun Zhang(张立军)

Chin. Phys. B, 2021, 30 (**1**): 016402. DOI: 10.1088/1674-1056/abd394

Growth and structural characteristics of metastable β-In_2Se_3 thin films on H-terminated Si(111) substrates by molecular beam epitaxy

Yi-Fan Shen(沈逸凡), Xi-Bo Yin(尹锡波), Chao-Fan Xu(徐超凡), Jing He(贺靖), Jun-Ye Li(李俊烨), Han-Dong Li(李含冬), Xiao-Hong Zhu(朱小红), Xiao-Bin Niu(牛晓滨)

Chin. Phys. B, 2020, 29 (**5**): 056402. DOI: 10.1088/1674-1056/ab820f

Structural transitions in $NaNH_2$ via recrystallization under high pressure

Yanping Huang(黄艳萍), Xiaoli Haung(黄晓丽), Xin Wang(王鑫), Wenting Zhang(张文亭), Di Zhou(周迪), Qiang Zhou(周强), Bingbing Liu(刘冰冰), Tian Cui(崔田)

Chin. Phys. B, 2019, 28 (**9**): 096402. DOI: 10.1088/1674-1056/ab37f8

Crystal melting processes of propylene carbonate and 1,3-propanediol investigated by the reed-vibration mechanical spectroscopy for liquids

Li-Na Wang(王丽娜), Xing-Yu Zhao(赵兴宇), Heng-Wei Zhou(周恒为), Li Zhang(张丽), Yi-Neng Huang(黄以能)

Chin. Phys. B, 2019, 28 (**9**): 096401. DOI: 10.1088/1674-1056/ab327d

Semiconductor-metal transition in GaAs nanowires under high pressure

Yi-Lan Liang(梁艺蓝), Zhen Yao(姚震), Xue-Tong Yin(殷雪彤), Peng Wang(王鹏), Li-Xia Li(李利霞), Dong Pan(潘东), Hai-Yan Li(李海燕), Quan-Jun Li(李全军), Bing-Bing Liu(刘冰冰), Jian-Hua Zhao(赵建华)

Chin. Phys. B, 2019, 28 (**7**): 076401. DOI: 10.1088/1674-1056/28/7/076401

Novel structures and mechanical properties of Zr_2N: *Ab initio* description under high pressures*

Minru Wen(文敏儒)[1], Xing Xie(谢兴)[1], Zhixun Xie(谢植勋)[1], Huafeng Dong(董华锋)[1,†], Xin Zhang(张欣)[1], Fugen Wu(吴福根)[2], and Chong-Yu Wang(王崇愚)[3,‡]

[1] *School of Physics and Optoelectronic Engineering, Guangdong University of Technology, Guangzhou* 510006, *China*
[2] *School of Materials and Energy, Guangdong University of Technology, Guangzhou* 510006, *China*
[3] *Department of Physics, Tsinghua University, Beijing* 100084, *China*

(Received 17 August 2020; accepted manuscript online 25 August 2020)

With the formation of structural vacancies, zirconium nitrides (key materials for cutting coatings, super wear-resistance, and thermal barrier coatings) display a variety of compositions and phases featuring both cation and nitrogen enrichment. This study presents a systematic exploration of the stable crystal structures of zirconium heminitride combining the evolutionary algorithm method and *ab initio* density functional theory calculations at pressures of 0 GPa, 30 GPa, 60 GPa, 90 GPa, 120 GPa, 150 GPa, and 200 GPa. In addition to the previously proposed phases $P4_2/mnm$-, *Pnnm*-, and *Cmcm*-Zr_2N, five new high-pressure Zr_2N phases of $P4/nmm$, $I4/mcm$, $P2_1/m$, $P\bar{3}m1$, and $C2/m$ are discovered. An enthalpy study of these candidate configurations reveals various structural phase transformations of Zr_2N under pressure. By calculating the elastic constants and phonon dispersion, the mechanical and dynamical stabilities of all predicted structures are examined at ambient and high pressures. To understand the structure–property relationships, the mechanical properties of all Zr_2N compounds are investigated, including the elastic moduli, Vickers hardness, and directional dependence of Young's modulus. The *Cmcm*-Zr_2N phase is found to belong to the brittle materials and has the highest Vickers hardness (12.9 GPa) among all candidate phases, while the $I4/mcm$-Zr_2N phase is the most ductile and has the lowest Vickers hardness (2.1 GPa). Furthermore, the electronic mechanism underlying the diverse mechanical behaviors of Zr_2N structures is discussed by analyzing the partial density of states.

Keywords: phase transition, phonon dispersion, Zr_2N, first-principles calculations

PACS: 64.60.−I, 63.20.D−, 81.05.Je, 71.15.Mb **DOI:** 10.1088/1674-1056/abb220

1. Introduction

As key materials for cutting coatings, super wear-resistance, and thermal barrier coatings, group IVB transition metal nitrides (TMNs; TM=Ti, Zr, and Hf) have been widely used in mold-making industries, automobile manufacturing, and aerospace industries owing to their high melting point, excellent chemical stability, corrosion resistance, and metallic conductivity.[1–4] In the TMNs, the well-known stable phase is the stoichiometric B_1-TMN compound with a rock-salt structure (space group $Fm\bar{3}m$). However, the TMNs may display a variety of compositions and phases featuring both cation and nitrogen enrichment.[5–8] Owing to the improvement of high-temperature and high-pressure experimental conditions, novel TMNs such as Th_3P_4-Zr_3N_4[9] and $I4/mcm$-TiN_2[10] have been experimentally synthesized and exhibit excellent mechanical properties. With metalloid vacancies displaying long- or short-range order, or both, most TMNs (TMN_x, for $x = 0$–1) exist on the metal-rich side (i.e., $x<0.5$) of the phase diagram.[5–7] However, compared to transition metal (TM) sub-nitrides, more research has focused on stoichiometric TMNs and nitrogen-rich TMNs. Consequently, an investigation of novel stable crystal structures for metal-rich TMNs under high pressure is essential for the development of practical applications.

Numerous studies exist on the phase stability, electronic structure, and mechanical properties of Ti-N,[11–17] Zr-N,[11–16,18–20] and Hf-N[12–16,18,21] systems. Recent studies using the evolutionary algorithm/search algorithm and density functional theory (DFT) have investigated the stable structures and possible stoichiometries of the TMN[15–17,20,21] systems. Yu *et al.*[17] explored the stable structures and possible stoichiometries of the Ti-N system at the pressures of 0 GPa, 20 GPa, and 60 GPa and found the new ground structures Ti_3N_2, Ti_4N_3, and Ti_6N_5 at atmospheric pressure and two novel stable phases *Cmcm*-Ti_2N and $I4/mcm$-TiN_2 at high pressures (synthesized by Bhadram *et al.* using the laser-heated diamond anvil cell technique at 73 GPa and 2400 K[10]). Weinberger *et al.*[15] investigated candidate stable structures of the group IVB and group VB TMNs at ambient pressure and demonstrated that the stable phase of Ti_2N and Zr_2N is the tetragonal $P4_2/mnm$ phase, while Hf_2N is more

*Project supported by the National Natural Science Foundation of China (Grant No. 11804057), the National Key R&D Program of China (Grant No. 2017YFB0701500), and the Natural Science Foundation of Guangdong, China (Grant Nos. 2017B030306003 and 2020A1515010862).

†Corresponding author. E-mail: hfdong@gdut.edu.cn
‡Corresponding author. E-mail: cywang@mail.tsinghua.edu.cn

© 2021 Chinese Physical Society and IOP Publishing Ltd

energetically favorable in the orthorhombic *Pnnm* phase. Research by Yu *et al.*[20] revealed that $Fm\bar{3}m$-ZrN, $P4_2/mnm$-Zr_2N, $C2/m$-Zr_4N_3, $C2/m$-Zr_6N_5, $C2/m$-Zr_8N_7, $P\bar{1}$-$Zr_{15}N_{16}$, $P\bar{1}$-Zr_7N_8, and $C2/m$-Zr_4N_5 are ground-state structures at 0 GPa and low temperatures. Zhang *et al.*[21] studied the pressure-composition phase diagram for the Hf-N system under 0–60 GPa and revealed new candidate phases with a Hf : N ratio of 6 : 1, 3 : 1, and 3 : 2 at zero pressure. Zirconium as well as Ti and Hf are group IVB TMs whose nitrides display similar phase transitions, chemical bonding, and elasticity. Unlike many studies for titanium and hafnium nitrides, the investigations of novel structural phases of high-pressure zirconium nitrides are limited. Specifically, no theoretical study has yet focused on new crystal structures of Zr-rich nitrides under high pressures.

Considering this background, the present research focuses on novel crystal configurations of zirconium sub-nitride Zr_2N at 0–200 GPa by combining evolutionary searches and first-principles calculations. By calculating the elastic constants and phonon spectra, the mechanical and dynamical stabilities for all candidate structures are evaluated. Additionally, the electronic and mechanical properties of the crystal phases are systematically analyzed to reveal the potential applications of the binary zirconium heminitrides.

2. Computational methods

To identify all potential novel Zr_2N crystal structures, the evolutionary algorithm method implemented in the USPEX code[22–24] with variable cell number (up to 30 atoms) is performed at pressures of 0 GPa, 30 GPa, 60 GPa, 90 GPa, 120 GPa, 150 GPa, and 200 GPa. We set the number of structures in the population to be 100, thus producing at random the first generation of structures. The 50 structures in the subsequent generations are produced by heredity (40%), soft mutation (20%), transmutation (20%), and randomness (20%).

The structural relaxations (i.e., optimization of lattice shape, volume, and atomic positions) and energies of every structure along with all calculations of the properties of interest are executed in the VASP code[25] based on DFT.[26,27] The projector augmented-wave method[28] is adopted for the ion-electron interactions, and the generalized gradient approximation of Perdew *et al.*[29] is used for the exchange-correlation function. Electrons in the $4s^24p^64d^25s^2$ and $2s^22p^3$ orbitals are considered as valence electrons for Zr and N, respectively. The plane-wave kinetic energy cutoff is set to 600 eV. Monkhorst-Pack[30] k-meshes with a resolution of $2\pi \times 0.04$ Å are adopted to characterize the energy integration in the Brillouin zone. The criteria for the force on the atoms are set at 0.01 eV/Å for ion self-consistency, while the energy convergence of the electronic self-consistency is set to be 10^{-5} eV per atom.

Using a $2 \times 2 \times 2$ supercell, the phonon dispersion relations are achieved in the framework of density functional perturbation theory[31,32] as implemented in the PHONOPY package[33] as well as the VASP code. The elastic constants are calculated by the strain–stress method,[34] and the elastic moduli (i.e., bulk modulus B, shear modulus G, and Young's modulus E) as well as Poisson's ratio ν, are obtained under the Voigt–Reuss–Hill approximation.[35–37] Employing Chen's model,[38] the theoretical Vickers hardness values are estimated using

$$H_v = 2(\kappa^2 G)^{0.585} - 3, \tag{1}$$

where $\kappa = G/B$ is the Pugh ratio. The directional dependence of Young's modulus is also calculated to reveal the anisotropy of all potential Zr_2N phases.

3. Results and discussion

Besides the known ε-Zr_2N (i.e., $P4_2/mnm$-Zr_2N), *Pnnm*-Zr_2N,[15,20] and *Cmcm*-Zr_2N phases, five novel phases (i.e., $P4/nmm$, $I4/mcm$, $P2_1/m$, $P\bar{3}m1$, and $C2/m$) of Zr_2N are predicted in this work via the evolutionary structure search and *ab initio* calculations. We note that, although there is no research reporting a *Cmcm*-type Zr_2N, the *Cmcm* phase has been discovered in titanium heminitride[17] and hafnium heminitride[21] at high pressure. Detailed crystallographic data and schematic crystal structures of all these phases at ambient pressure are shown in Table 1 and Fig. 1, respectively. Noticeably, our evolutionary simulations successfully identify the well-known ε-Zr_2N phase, representing the reported stable structure for zirconium heminitride at 0 GPa by Yu *et al.*[20] Additionally, the calculated equilibrium lattice constants for $P4_2/mnm$-Zr_2N ($a = b = 5.422$ Å, $c = 3.307$ Å) are consistent with the DFT-obtained values previously reported in Ref. [20]. Similar to the scenario represented by the ε-Ti_2N and *Pnnm*-Hf_2N phases,[15] we note that *Pnnm*-Zr_2N is a distorted version of ε-Zr_2N with lower crystal structure symmetry. To more easily observe this distortion, the crystal structures of $P4_2/mnm$-Zr_2N and *Pnnm*-Zr_2N viewed along the a-axis (i.e., [100] direction) are plotted in the lower panels of Figs. 1(a) and 1(b), respectively. By drawing the Zr–N bonds, the bond angles in the $P4_2/mnm$-Zr_2N phase can be seen as axially symmetric along the [110] and $[\bar{1}10]$ directions, while these symmetries are absent in *Pnnm*-Zr_2N and the bond angles display subtle distortions. It can be expected that the bonding character and mechanical behaviors of the *Pnnm*-phase will be similar to those of ε-Zr_2N.

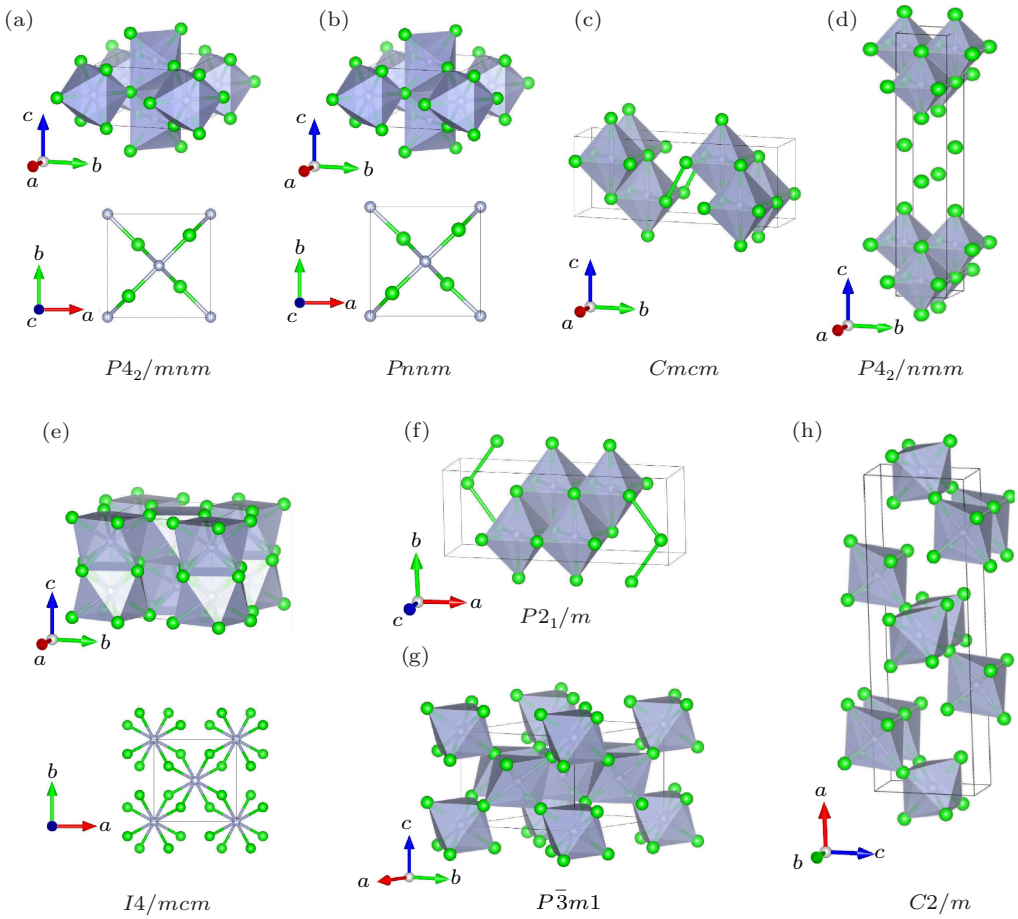


Fig. 1. Schematic crystal structures of potential Zr_2N for (a) $P4_2/mnm$, (b) $Pnnm$, (c) $Cmcm$, (d) $P4/nmm$, (e) $I4/mcm$, (f) $P2_1/m$, (g) $P\bar{3}m1$, and (h) $C2/m$ phases at 0 GPa. The schematic shows the N atoms (gray circles) in the centers of the gray polyhedrals and the Zr atoms (green circles).

As displayed in Fig. 1, although the $Cmcm$, $P4/nmm$, and $P2_1/m$ phases belong to different crystal systems and have different symmetries, they demonstrate similar characters wherein all N atoms are octahedrally coordinated by six Zr atoms and the NZr_6 octahedrons arrange along a uniform direction. In fact, the $Cmcm$, $P4/nmm$, and $P2_1/m$ phases are versions of the rocksalt B_1-TiN (space group $Fm\bar{3}m$, No. 225) with ordered N-vacancies. Likewise, vacancy-ordered phases have also been reported for group IVB TMNs[17,21] and carbides.[39,40] In the $P\bar{3}m1$ and $C2/m$ phases, N atoms are also centered in the octahedron (composed of Zr atoms) interstices, though NZr_6 octahedrons arrange along different orientations. There are 12 atoms in a unit cell of the anti-rutile structure of the $I4/mcm$ phase, of which the metal Zr and nonmetal N atoms occupy the Wyckoff 8h and 4a positions, respectively. Each N atom is coordinated by eight Zr atoms, forming a decahedron. This crystal structure naturally reminds us of the $I4/mcm$-TiN_2 phase belonging to the same space group, where the metal atoms and nitrogen atoms in $I4/mcm$-TiN_2 and $I4/mcm$-Zr_2N phases occupy the opposite Wyckoff positions. However, unlike the short NN dumbbell bond length of $I4/mcm$-ZrN_2, which is as short as 1.424 Å at 1 atm,[16] the Zr–Zr bond length of $I4/mcm$-Zr_2N is as long as 2.981 Å at ambient pressure. It can therefore be predicted that the mechanical strength and hardness of $I4/mcm$-Zr_2N will be significantly less than those of $I4/mcm$-ZrN_2.

To ascertain the thermodynamic stability of the predicted Zr_2N configurations, we obtain the formation enthalpies per atom ΔH using

$$\Delta H = \left[H(\mathrm{Zr_2N}) - 2H(\mathrm{Zr}) - \frac{1}{2}H(\mathrm{N_2})\right]/3, \qquad (2)$$

where $H(Zr_2N)$, $H(Zr)$, and $H(N_2)$ are the enthalpies per formula unit of Zr_2N, $P63/mcm$-Zr, and α-N_2, respectively, at a specific pressure. Our determined formation enthalpies of all Zr_2N candidate phases at 0 GPa are summarized in Table 1. It can be seen that $P4_2/mnm$-Zr_2N is the most stable phase of zirconium heminitride at atmospheric pressure with the formation enthalpy calculated to be -1.2914 eV per atom, which agrees well with the result of -1.249 eV/atom from Ref. [21]. As a distorted version of ε-Zr_2N (see Figs. 1(a) and 1(b)), we note that the ΔH of the $Pnnm$ phase is only slightly higher than that of $P4_2/mnm$-Zr_2N. As shown in Table 1, the $I4/mcm$ phase exhibits the highest formation enthalpy among the eight phases, indicating that $I4/mcm$ Zr_2N is the least energetically favorable phase for zirconium heminitride at 0 GPa.

Table 1. Structural parameters (lattice constants and atomic coordinates) and formation enthalpies ΔH of the candidate phases of Zr_2N at 0 GPa, along with other DFT-predicted values.

Phases	Lattice parameters (Å, degree)	Wyckoff positions					ΔH (eV·atom^{-1})
		atom	site	x	y	z	
$P4_2/mnm$	$a=b=5.422$, $c=3.307$	Zr	4g	0.796	0.796	0.500	−1.2914
	$a=b=5.426$[a], $c=3.319$[a]	N	2a	0.00	0.00	0.00	−1.249[b]
$Pnnm$	$a=5.449$, $b=5.397$	Zr	4g	0.302	0.209	0.00	−1.2912
	$c=3.305$	N	2c	0.500	0.00	0.500	
$Cmcm$	$a=3.244$, $b=12.468$	Zr1	4c	0.00	0.187	0.75	−1.2708
	$c=4.771$	Zr2	4c	0.500	0.064	0.25	
		N	4c	0.00	0.186	0.25	
$P4/nmm$	$a=b=3.252$, $c=18.049$	Zr1	8j	0.00	0.500	0.934	−1.2041
		Zr2	8j	0.00	0.500	0.440	
		Zr3	8j	.00	0.500	0.189	
		Zr4	8j	0.500	0.00	0.318	
		N1	8j	0.00	0.500	0.063	
		N2	8j	0.00	0.500	0.809	
$I4/mcm$	$a=b=5.721$, $c=5.437$	Zr	8h	0.324	0.824	0.500	−0.6913
		N	4a	0.500	0.500	0.75	
$P2_1/m$	$a=12.511$, $b=4.733$	Zr1	2e	0.949	0.25	0.751	−1.2170
	$c=3.241$	Zr2	2e	0.434	0.25	0.250	
	$\alpha=\gamma=90$, $\beta=89.944$	Zr4	2e	0.813	0.75	0.749	
		N1	2e	0.693	0.75	0.249	
		N2	2e	0.434	0.75	0.250	
$P\bar{3}m1$	$a=b=6.544$, $c=5.224$	Zr1	6i	0.166	0.332	0.253	−1.2576
	$\alpha=\beta=90$, $\gamma=120$	Zr2	2d	0.333	0.667	0.733	
		N1	3f	0.500	0.500	0.500	
		N2	1a	0.00	0.00	0.00	
$C2/m$	$a=16.598$, $b=3.313$	Zr1	4i	0.898	0.500	0.206	−1.2803
	$c=5.331$	Zr2	4i	0.563	0.500	0.291	
	$\alpha=\gamma=90$, $\beta=91.993$	Zr3	4i	0.730	0.00	0.241	
		N1	4i	0.834	0.00	0.979	
		N2	2d	0.500	0.00	0.500	

[a]Ref. [20], [b]Ref. [15].

To further investigate the phase transition of Zr_2N at high pressure, the enthalpies of these candidate configurations are calculated as a function of pressure up to 200 GPa. Figure 2 plots the calculated enthalpy (relative to the *Cmcm* phase) per atom as a function of pressure for all candidate phases and the inset shows a detail of the enthalpy-pressure curves for the 3–17 GPa pressure range. As demonstrated in Fig. 2, the diverse crossings between different structures in the pressure range of 0–200 GPa indicate the existence of various structural phase transformations for Zr_2N under pressure. The $P4_2/mnm$-Zr_2N transforms to $Pnnm$-Zr_2N at approximately 6.5 GPa, whereupon $Pnnm$-Zr_2N transforms to $Cmcm$-Zr_2N at 16.3 GPa. This is different from the scenario of Ti_2N and Hf_2N. Specifically, the stable crystal structure of titanium heminitride at the ambient pressure (i.e., $P4_2/mnm$-Ti_2N) transforms directly to $Cmcm$-Ti_2N at 20.8 GPa.[17] In terms of hafnium heminitride, the orthorhombic $Pnnm$-Hf_2N phase, which is the most stable configuration at atmospheric pressure, transforms to $Cmcm$-Hf_2N at 12.5 GPa.[21] According to Fig. 2, though the $Cmcm$-Zr_2N is initially the most energetically favorable when the pressure exceeds 16.3 GPa, other phases become more energetically favorable as the pressure increases further. For example, the $P4/nmm$-Zr_2N phase exhibits a lower enthalpy than $Cmcm$-Zr_2N at 55.2 GPa, as does the $P2_1/m$-Zr_2N phase at 65.0 GPa, where the $P4/nmm$-Zr_2N phase possesses the lowest enthalpy from 55.2 GPa to 144.4 GPa. When the pressure further increases, the $P4/nmm$ and $P2_1/m$ phases both transform to the $I4/mcm$ configuration at pressures of 122.8 GPa and 144.4 GPa, respectively. This signifies that the $I4/mcm$-Zr_2N phase is the most energetically-favored structure in the 144.4–200 GPa pressure range. The enthalpies of the $P\bar{3}m1$ and $C2/m$ phases are higher than those of the $Pnnm$ phase during the entire studied pressure range, but these phases possess a lower enthalpy than the $P4_2/mnm$ phase when the pressure exceeds 34.5 GPa and 40.3 GPa, respectively.

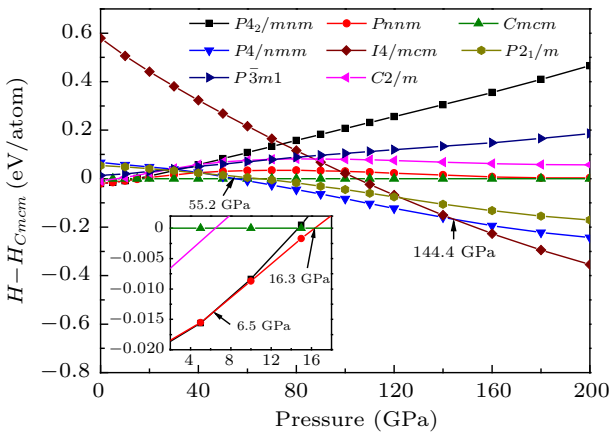


Fig. 2. Calculated enthalpy curves as a function of pressure for the different phases of Zr_2N, with reference to the *Cmcm* phase. Inset: Detail of the enthalpy–pressure curves in the 3–17 GPa pressure range.

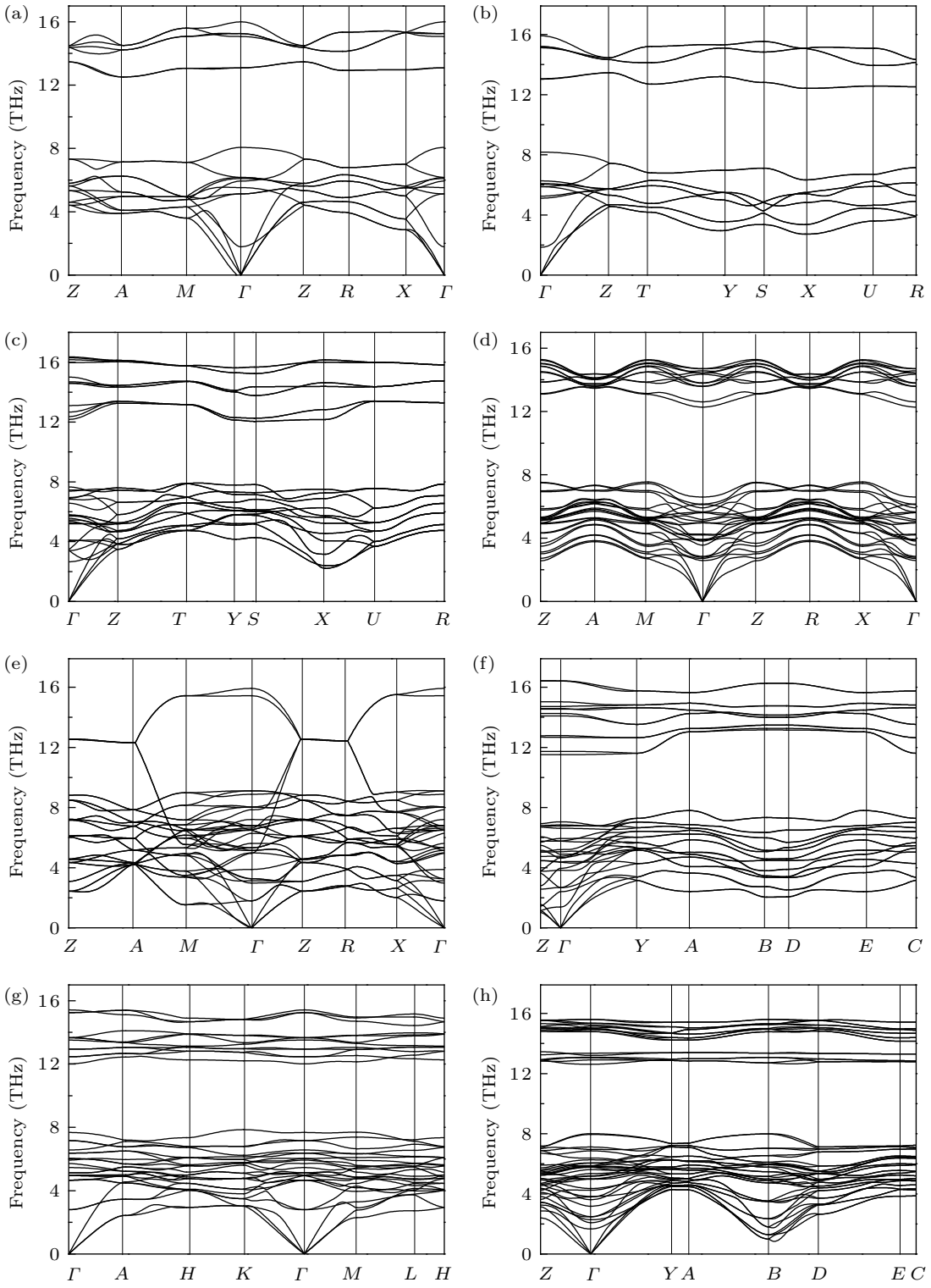


Fig. 3. Phonon dispersion curves for (a) $P4_2/mnm$, (b) $Pnnm$, (c) $Cmcm$, (d) $P4/nmm$, (e) $I4/mcm$, (f) $P2_1/m$, (g) $P\bar{3}m1$, and (h) $C2/m$ phases at 0 GPa, respectively.

Next, the dynamical and mechanical stabilities of the candidate Zr_2N structures are investigated using the phonon spectra and elastic constants. The calculated phonon frequencies of the five novel structures ($P4/nmm$, $I4/mcm$, $P2_1/m$, $P\bar{3}m1$, and $C2/m$) and the $P4_2/mnm$, $Pnnm$, and $Cmcm$ phases of Zr_2N at atmospheric pressure are plotted in Fig. 3. Clearly, there are no imaginary frequencies for all predicted phases at 0 GPa, signifying that these configurations are all dynamically stable. The calculated phonon dispersion curves of $P4_2/mnm$-Zr_2N in this study are consistent with previous DFT results.[20] In addition to ambient pressure, we also study the phonon stability of all structures under high pressure. Soft phonons are found in ε-Zr_2N, $P4/nmm$-Zr_2N, and $C2/m$-Zr_2N with an initial negative slope at the Γ point (related to crystal instability under a

homogeneous deformation) for pressures of 20 GPa, 200 GPa, and 120 GPa, respectively. This suggests the existence of mechanical instability in ε-Zr_2N, $P4/nmm$-Zr_2N, and $C2/m$-Zr_2N at these corresponding pressures.[41] The *Cmcm*, *I*4/*mcm*, and $P2_1/m$ phases, however, maintain their phonon stability above 200 GPa, while the *Pnnm* and $P\bar{3}m1$ configurations hold dynamic stability up to 200 GPa and 160 GPa, respectively.

The elastic constants were obtained using the strain-stress method and are summarized in Table 2. The $P4_2/mnm$, *P*4/*nmm*, and *I*4/*mcm* structures belong to the tetragonal crystal system (Laue class of 4/*mmm*) and have six independent elastic constants. The mechanical stability criteria of the tetragonal crystal are given as[42–44]

$$C_{11} > |C_{12}|, C_{44} > 0, C_{66} > 0, C_{33}(C_{11}+C_{12}) > 2C_{13}^2. \quad (3)$$

The *Pnnm*- and *Cmcm*-Zr_2N are both orthorhombic crystal systems with nine independent elastic constants. The mechanical stability criteria for an orthorhombic class are[45]

$$\begin{aligned} &C_{11} > 0,\ \ C_{44} > 0,\ \ C_{55} > 0,\\ &C_{66} > 0,\ \ C_{11}C_{22} > C_{12}^2,\\ &C_{11}C_{22}C_{33} + 2C_{12}C_{13}C_{23} - C_{11}C_{23}^2\\ &-C_{22}C_{13}^2 - C_{33}C_{12}^2 > 0. \end{aligned} \quad (4)$$

With thirteen independent C_{ij}, the mechanical stability criteria of the two monoclinic Zr_2N phases (i.e., $P2_1/m$ and $C2/m$) are given by[46]

$$\begin{aligned} &C_{11} > 0,\ \ C_{44} > 0,\ \ C_{11}C_{22} - C_{12}^2 > 0,\ \ C_{44}C_{66} - C_{46}^2 > 0,\\ &T = C_{11}C_{22}C_{33} + 2C_{12}C_{13}C_{23} - C_{11}C_{23}^2\\ &\quad -C_{22}C_{13}^2 - C_{33}C_{12}^2 > 0,\\ &C_{15}^2(C_{23}^2 - C_{22}C_{33}) + C_{25}^2(C_{13}^2 - C_{11}C_{33})\\ &+C_{35}^2(C_{12}^2 - C_{11}C_{22}) + 2C_{15}C_{35}(C_{13}C_{22} - C_{12}C_{23})\\ &+2C_{15}C_{25}(C_{12}C_{33} - C_{13}C_{23})\\ &+2C_{25}C_{35}(C_{23}C_{11} - C_{12}C_{13}) + C_{55}T > 0. \end{aligned} \quad (5)$$

The $P\bar{3}m1$-Zr_2N phase belongs to the trigonal crystal system (Laue class of $\bar{3}m$) and has six independent elastic constants. The mechanical stability criteria of a trigonal crystal are[47]

$$\begin{aligned} &C_{11} > |C_{12}|,\ \ C_{33} > 0,\ \ C_{44} > 0,\\ &(C_{11}+C_{12})C_{33} > 2C_{13}^2,\ (C_{11}-C_{12})C_{44} > 2C_{14}^2. \end{aligned} \quad (6)$$

According to Table 2, the calculated elastic constants of the eight candidate Zr_2N phases all satisfy the mechanical stability criteria, indicating that these Zr_2N configurations are mechanically stable at ambient pressure. The above discussions of phonons reveal that $P4_2/mnm$-, $C2/m$-, and *P*4/*nmm*-Zr_2N will exhibit mechanical instability at 20 GPa, 120 GPa, and 200 GPa, respectively. We calculate the C_{ij} values and examine the mechanical stability criteria of a tetragonal crystal using Eq. (3), and find that the lattice of $P4_2/mnm$ phase becomes mechanically unstable when $C_{11}<C_{12}$ at 20 GPa, while the mode of failure for the *P*4/*nmm* structure is $C_{33}(C_{11}+C_{12}) < 2C_{13}^2$ at 200 GPa. In terms of $C2/m$ phase, the lattice is found to become mechanically unstable in the $C_{44}<0$ mode at 120 GPa according to Eq. (5).

Table 2. Calculated elastic constants (C_{ij}), elastic moduli (i.e., bulk modulus B_H, shear modulus G_H, and Young's modulus E), B/G ratio, Poisson's ratio (v), and Vickers hardness (H_v) of the Zr_2N compounds at zero pressure, along with other DFT calculated values. C_{ij}, B_H, G_H, E, and H_v are in GPa, B/G, and v are dimensionless.

Phase	$P4_2/mnm$			*Pnnm*	*Cmcm*	*P*4/*nmm*	*I*4/*mcm*	$P2_1/m$	$P\bar{3}m1$	*C*2/*m*
C_{11}	248.9	305[a]	232[b]	234.4	334.1	289.5	225.6	207.8	291.4	272.5
C_{12}	169.0	142[a]	163[b]	178.4	69.9	119.9	176.6	108.3	105.0	100.0
C_{13}	97.8	108[a]	107[b]	109.1	72.2	94.7	96.5	75.6	91.7	135.0
C_{14}									7.1	
C_{15}								−3.9		−32.4
C_{22}				240.3	259.7			261.5		336.5
C_{23}				86.8	84.4			68.9		76.6
C_{25}								0.8		14.4
C_{33}	358.3	362[a]	348[b]	355.0	259.4	150.8	278.6	318.3	264.5	256.5
C_{35}								0.9		28.6
C_{44}	119.1	119[a]	114[b]	118.3	103.6	81.0	42.2	78.0	70.9	105.4
C_{46}								0.0		3.5
C_{55}				118.8	88.8			17.0		69.3
C_{66}	117.0	114[a]	120[b]	117.1	60.1	99.5	81.5	70.2	93.2	121.7
B_H	175.9	187[a]	173[b]	175.1	144.6	140.8	163.1	142.7	157.9	164.6
G_H	94.7	109[a]	88[b]	87.3	89.8	77.5	51.1	56.8	83.3	86.7
E	240.8	274[a]	227[b]	224.5	223.2	196.4	138.8	150.4	212.4	221.3
v	0.272	0.256[a]	0.28[b]	0.286	0.243	0.268	0.358	0.324	0.276	0.276
B/G	1.859	1.721[a]	1.966[b]	2.006	1.610	1.818	3.191	2.514	1.897	1.898
H_v	10.9	13.5[a]	9.5[b]	9.1	12.9	9.7	2.1	4.2	9.6	9.9

[a]Ref. [20], [b]Ref. [48].

The constants C_{11}, C_{22}, and C_{33} reflect the resistance of the crystal to normal strain in the [100], [010], and [001] directions, respectively. As mentioned above, the *Cmcm*, *P*4/*nmm*, and $P2_1/m$ phases are versions of the cubic *B*1-TiN possessing ordered nitrogen vacancies. As shown in Table 2, $P2_1/m$-Zr_2N possesses the lowest C_{11} among the eight predicted structures. This is because the N-vacancies of the $P2_1/m$ phase are distributed in the (100) plane and the least-dense atomic arrangement is in the [100] direction (see Fig. 1). Similarly, the N-vacancies of the *P*4/*nmm* phase are distributed in the (001) plane and the atomic compactness in the [001] direction is the worst (shown in Fig. 1). The *P*4/*nmm*-Zr_2N phase possesses the lowest C_{33} value among the eight candidate structures. Conversely, the *Cmcm*, $C2/m$, and $P4_2/mnm$ phases respectively exhibit the highest C_{11}, C_{22}, and C_{33} values. We note that our calculated elastic constants (except C_{11}) of $P4_2/mnm$-Zr_2N are consistent with the results of Yu *et al.*,[20] and our calculated C_{11} of ε-Zr_2N agrees well with the result of Ref. [48].

The elastic moduli (i.e., bulk modulus B_H, shear modulus G_H, and Young's modulus E), B/G ratio, Poisson's ratio v, and Vickers hardness H_v of the Zr_2N compounds at zero pressure are further studied by the methods mentioned in Secion 2 and are summarized in Table 2. Clearly, ε-Zr_2N exhibits the largest bulk, shear, and Young's moduli among the Zr_2N compounds, which indicates that ε-Zr_2N has the best resistance to volume change and shear shape deformation, and the best stiffness. Notably, the *Pnnm* phase, which is a distorted version of the ε-Zr_2N phase, has similar but lower elastic moduli compared with those of the ε phase. The *P*4/*nmm*-Zr_2N phase exhibits the smallest B_H value, while *I*4/*mcm*-Zr_2N possesses the smallest G_H and E values.

The B/G ratios (proposed by Pugh[49]) of all structures except the *Cmcm* phase are larger than 1.75, implying that the $P4_2/mnm$, *Pnnm*, *P*4/*nmm*, *I*4/*mcm*, $P2_1/m$, $P\bar{3}m1$, and $C2/m$ phases belong to ductile materials, where the *I*4/*mcm* phase is the most ductile among these configurations. In contrast, *Cmcm*-Zr_2N possesses the smallest B/G ratio and Poisson's ratio v, which is the most brittle phase among the Zr_2N compounds. Intriguingly, owing to its brittleness, *Cmcm*-Zr_2N exhibits the highest Vickers hardness (12.9 GPa), though its shear modulus is lower than that of ε-Zr_2N. Contrarily, the *I*4/*mcm* phase has the lowest hardness as small as 2.1 GPa at ambient pressure. Note here that the *I*4/*mcm* phase has the lowest shear modulus, Young's modulus, and hardness among the studied structures, where its abnormal and relatively higher bulk modulus primarily originates from its large mass density.

Moreover, we investigate the directional dependence of Young's modulus for all predicted Zr_2N phases (see Fig. 4). Although the eight candidate configurations possess identical chemical composition ratios, their mechanical properties exhibit considerable differences. Young's modulus of the $P\bar{3}m1$ phase displays the most isotropic features among the Zr_2N compounds because its three-dimensional Young's modulus diagram shape is the closest to a sphere. Looking at the diagram shapes in Fig. 4 and the degree of their deviation from spherical, the $P2_1/m$-Zr_2N phase exhibits the most anisotropic features, followed by the *Pnnm* and *I*4/*mcm* phases. The anisotropy of the $P2_1/m$-Zr_2N arises from the high C_{33} and C_{22} values and the low C_{23} value, resulting in a large Young's modulus in the y- and z-axis directions and a small E in the diagonal directions of the y–z plane. The anisotropy of the *Pnnm* and *I*4/*mcm* phases is mainly owing to their relatively low C_{11} and C_{22} values and high C_{12} value, resulting in a small Young's modulus in the x- and y-axis directions and a large E in the diagonal directions of the x–y plane.

To understand the electronic properties and bonding features of these zirconium heminitrides, we further study the density of states (DOS) of each system. Figure 5 shows the s- and p-orbital partial DOS of N, the d-orbital partial DOS of Zr, and the total DOS for all Zr_2N phases. Notably, all Zr_2N compounds are metallic owing to the finite DOS at the Fermi level, which are dominated by the 4d orbitals of the zirconium atoms (see Fig. 5). Owing to the contribution of the 2s orbitals of the N atoms, all studied configurations exhibit a deep valence band below -12 eV. Similar to the scenario reported in the $Ti_{n+1}N_n$ ($n = 1$, 2, 3, and 5) structures,[17] interactions exist here between Zr and N atoms. According to Fig. 5, these interactions originate from the hybridization of the N-2p states and Zr-4d states in the energy region of -7 eV to -2.5 eV. We note that the interaction between Zr and N in the *Cmcm* phases exhibits greater hybridization than that in the *P*4/*nmm* and $P2_1/m$ structures. This suggests that *Cmcm*-Zr_2N will possess better mechanical strength and deformation resistance than the *P*4/*nmm* and $P2_1/m$ phases, which is consistent with the calculated results of the elastic moduli in Table 2. Unlike the strong covalent N–N bonding nature in the *I*4/*mcm*-type TM pernitrides, weaker interactions are exhibited by the covalent-like Zr–N bond and metallic Zr–Zr bond in the *I*4/*mcm*-Zr_2N phase. Consequently, compared with *I*4/*mcm*-type TM pernitrides, the *I*4/*mcm*-type TM heminitrides possess reduced mechanical strength and hardness. For example, compared with the values exhibited by *I*4/*mcm*-Zr_2N, the *I*4/*mcm*-ZrN_2 structure exhibits larger calculated bulk modulus (1.7×), shear modulus (3.4×), Young's modulus (3.1×), and hardness (12.3×).[16]

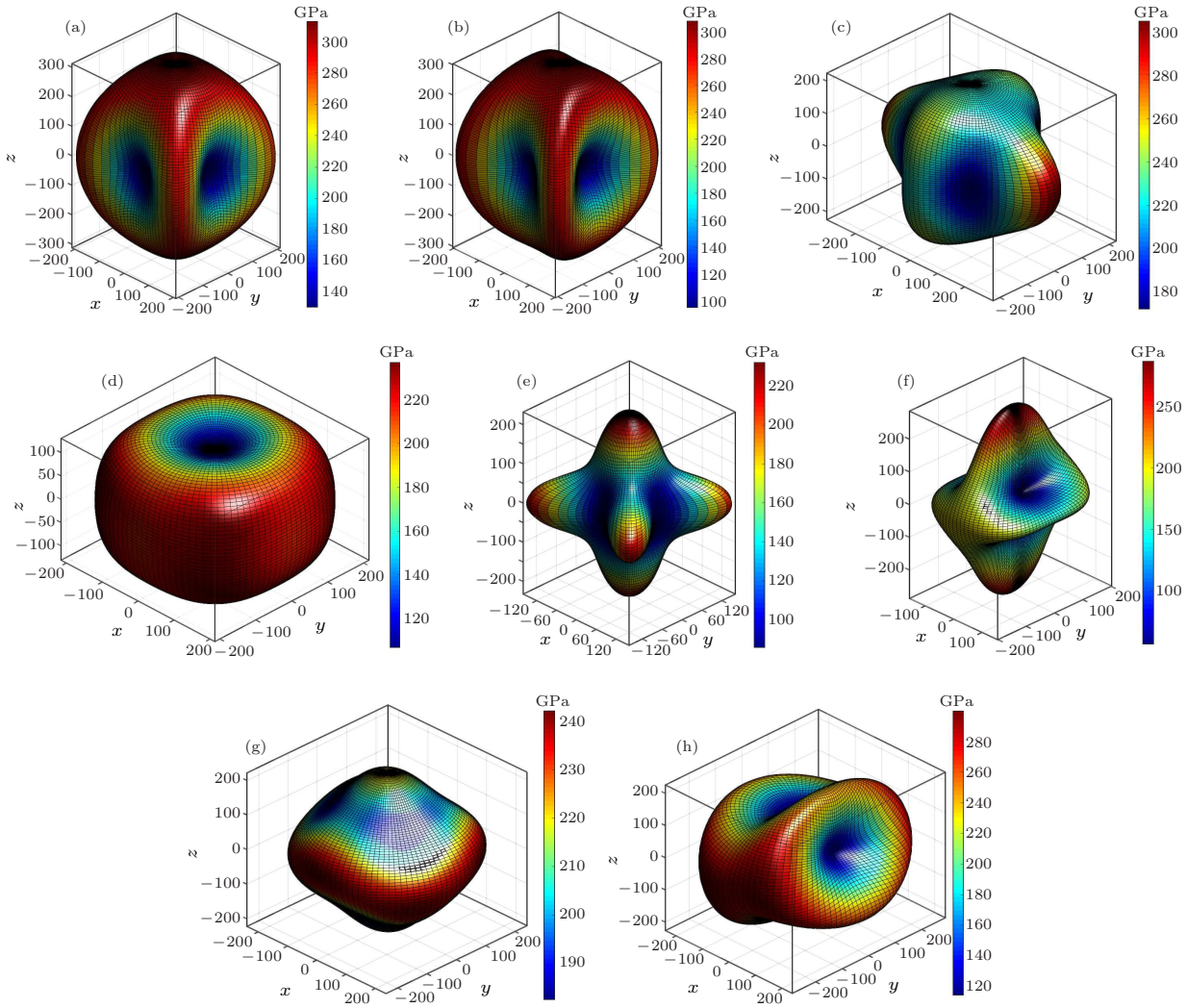


Fig. 4. Directional dependence of Young's modulus (in GPa) of (a) $P4_2/mnm$, (b) $Pnnm$, (c) $Cmcm$, (d) $P4/nmm$, (e) $I4/mcm$, (f) $P2_1/m$, (g) $P\bar{3}m1$, and (h) $C2/m$ phases at 0 GPa.

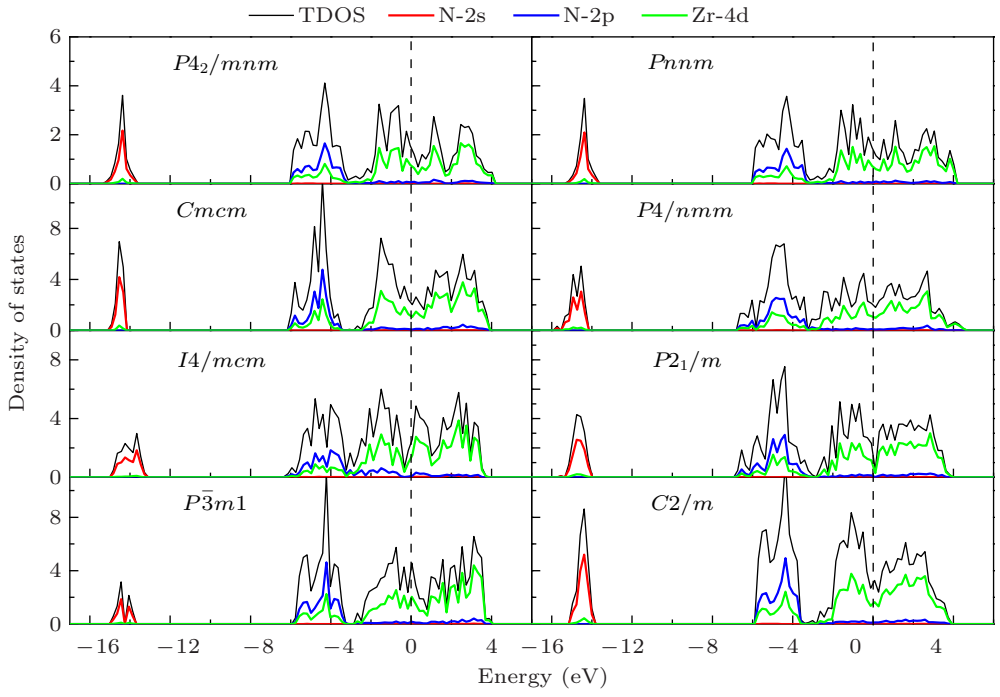


Fig. 5. Projected density of states (DOS) of Zr_2N compounds at ambient pressure, showing the partial DOS of the N 2s (red line) and N 2p (blue line) orbitals, the Zr 4d orbital (green line), and the total DOS (black line).

4. Conclusion

In summary, the pressure-dependent phase diagram of zirconium heminitride is investigated using *ab initio* evolutionary algorithm methods. Five novel high-pressure phases (i.e., $P4/nmm$, $I4/mcm$, $P2_1/m$, $P\bar{3}m1$, and $C2/m$) of Zr_2N are predicted in the present study. As the pressure increases from 0 GPa to 200 GPa, Zr_2N moves sequentially through the phases as $P4_2/mnm \rightarrow Pnnm \rightarrow Cmcm \rightarrow P4/nmm \rightarrow I4/mcm$ at the corresponding transition pressures of 6.5 GPa, 16.3 GPa, 55.2 GPa, and 144.4 GPa, respectively. The calculated phonon spectra reveal that all candidate Zr_2N structures are dynamically stable at ambient pressure. According to the calculated elastic constants, all predicted Zr_2N configurations are expected to be mechanically stable at atmospheric pressure. Although the eight candidate configurations possess identical chemical composition ratios, their mechanical properties exhibit considerable differences. Excepting the *Cmcm* phase, the Zr_2N structures are ductile materials, among which the *I4/mcm* phase is the most ductile configuration. At atmospheric pressure, the Vickers hardness of the Zr_2N compounds is ordered as $Cmcm > P4_2/mnm > C2/m > P4/nmm > P\bar{3}m1 > Pnnm > P2_1/m > I4/mcm$. The calculated electronic structures demonstrate that the high mechanical strength and hardness of the *Cmcm* phase originate from the strong hybridization of the N-2p states and Zr-4d states, while the weaker interactions between the Zr and N atoms are likely responsible for the weaker mechanical behaviors of $I4/mcm$-Zr_2N. These results provide important additional insight into the structure-property relationships of TM heminitrides and the development of practical applications for Zr_2N.

Acknowledgment

We thank Sara Maccagnano-Zacher, PhD, from Liwen Bianji, Edanz Editing China (www.liwenbianji.cn/ac), for editing the English text of a draft of this manuscript.

References

[1] Musil J 2000 *Surface & Coatings Technology* **125** 322
[2] Gotoh Y, Fujiwara S and Tsuji H 2016 *Journal of Vacuum Science & Technology A: Vacuum, Surfaces, and Films* **34** 031401
[3] Siow P C, A. Ghani J, Ghazali M J, Jaafar T R, Selamat M A and Che Haron C H 2013 *Ceramics International* **39** 1293
[4] Sue J A and Troue H H 1991 *Surface & Coatings Technology* **49** 31
[5] Ogawa T 1994 *J. Alloys Compd.* **203** 221
[6] Gusev A I and Rempel A A 1997 *Physica Status Solidi (a)* **163** 273
[7] Wang W E and Olander D R 1995 *Journal of Alloys and Compounds* **224** 153
[8] Pierson H O 1997 *Handbook of Refractory Carbides and Nitrides: Properties, Characteristics, Processing and Applications* (New York: Noyes Publication)
[9] Zerr A, Miehe G and Riedel R 2003 *Nat. Mater.* **2** 185
[10] Bhadram V S, Kim D Y and Strobel T A 2016 *Chemistry of Materials* **28** 1616
[11] Brik M G and Ma C G 2012 *Computational Materials Science* **51** 380
[12] Srivastava A, Chauhan M and Singh R K 2011 *Physica Status Solidi* **248** 2793
[13] Chauhan M and Gupta D C 2014 *International Journal of Refractory Metals and Hard Materials* **42** 77
[14] Wang A J, Shang S L, Zhao D D, Wang J, Chen L, Du Y, Liu Z K, Xu T and Wang S Q 2012 *Calphad-Comput. Coupling Ph. Diagrams Thermochem.* **37** 126
[15] Weinberger C R, Yu X X, Yu H and Thompson G B 2017 *Computational Materials Science* **138** 333
[16] Yu R, Sun E, Jiao L, Cai Y, Wang H and Yao Y 2018 *RSC Advances* **8** 36412
[17] Yu S, Zeng Q, Oganov A R, Frapper G and Zhang L 2015 *Phys. Chem. Chem. Phys.* **17** 11763
[18] Bazhanov D I, Knizhnik A A, Safonov A A, Bagatur'yants A A, Stoker M W and Korkin A A 2005 *J. Appl. Phys.* **97** 044108
[19] Durandurdu M 2019 *Philosophical Magazine* **99** 942
[20] Yu S, Zeng Q, Oganov A R, Frapper G, Huang B, Niu H and Zhang L 2017 *RSC Advances* **7** 4697
[21] Zhang J, Oganov A R, Li X and Niu H 2017 *Phys. Rev. B* **95** 020103
[22] Oganov A R and Glass C W 2006 *J. Chem. Phys.* **124** 244704
[23] Oganov A R, Lyakhov A O and Valle M 2011 *Accounts of Chemical Research* **44** 227
[24] Oganov A R, Ma Y, Lyakhov A O, Valle M and Gatti C 2010 *Reviews in Mineralogy & Geochemistry* **71** 271
[25] Kresse G and Furthmüller J 1996 *Phys. Rev. B* **54** 11169
[26] Hohenberg P and Kohn W 1964 *Phys. Rev.* **136** B864
[27] Kohn W and Sham L J 1965 *Phys. Rev.* **140** A1133
[28] Kresse G and Joubert D 1999 *Phys. Rev. B* **59** 1758
[29] Perdew J P, Burke K and Ernzerhof M 1996 *Phys. Rev. Lett.* **77** 3865
[30] Monkhorst H J and Pack J D 1976 *Phys. Rev. B* **13** 5188
[31] Baroni S, De Gironcoli S, Dal Corso A and Giannozzi P 2001 *Rev. Mod. Phys.* **73** 515
[32] Baroni S and Resta R 1986 *Phys. Rev. B* **33** 7017
[33] Togo A, Oba F and Tanaka I 2008 *Phys. Rev. B* **78** 134106
[34] Shang S, Wang Y and Liu Z K 2007 *Appl. Phys. Lett.* **90** 101909
[35] Hill R 1952 *Proc. Phys. Soc. Sect. A* **65** 349
[36] Voigt W 1928 *Lehrbuch der Kristallphysik* (Leipzig Berlin: Ann Arbor, Mich)
[37] Reuss A 1929 *J. Appl. Mathematics Mech.* **9** 49
[38] Chen X Q, Niu H, Li D and Li Y 2011 *Intermetallics* **19** 1275
[39] Zeng Q, Peng J, Oganov A R, Zhu Q, Xie C, Zhang X, Dong D, Zhang L and Cheng L 2013 *Phys. Rev. B* **88** 214107
[40] Jiang C and Jiang W 2014 *Physica Status Solidi (b)* **251** 533
[41] Clatterbuck D M, Krenn C R, Cohen M L and Morris Jr J W 2003 *Phys. Rev. Lett.* **91** 135501
[42] Milstein F 1971 *Phys. Rev. B* **3** 1130
[43] Nye J F 1985 *Physical Properties of Crystals: Their Representation by Tensors and Matrices* (New York: Oxford University Press)
[44] Wang H and Li M 2010 *J. Phys.: Condens. Matter* **22** 295405
[45] Mouhat F and Coudert F X 2014 *Phys. Rev. B* **90** 224104
[46] Wen M, Xie X, Gao Y, Dong H, Mu Z, Wu F and Wang C Y 2019 *J. Alloys and Compd.* **806** 1260
[47] Tsuchiya T, Yamanaka T and Matsui M 2000 *Physics and Chemistry of Minerals* **27** 149
[48] Winston D and Jong M D *Materials Project*
[49] Pugh S F 1954 *The London, Edinburgh, and Dublin Philosophical Magazine and Journal of Science* **45** 823